A Low-Profile High-Efficiency Transmitarray Antenna Reflecting Effective Phase Discontinuity With TE/TM Superimpose Analysis

Uichan Park, *Graduate Student Member, IEEE*, Jinhyun Kim, *Graduate Student Member, IEEE*, Taeyeong Yoon, *Graduate Student Member, IEEE*, Haeseung Lee, *Member, IEEE*, Kyungho Yoo, *Member, IEEE*, and Jungsuek Oh, *Senior Member, IEEE*

***Abstract*— In this study, we propose a high-efficiency, low-profile transmitarray (TA) antenna system and present an efficient design procedure by co-designing a multiport subarray antenna (MPSA) to perform as a feed source and the TA simultaneously. The proposed TA antenna supports dual slant polarization (SP). Furthermore, the concept of effective phase discontinuity (EPD) based on a mutual coupling coefficient is introduced for efficient TA design operation at short focal lengths to verify the effectiveness of the advanced unit cell (UC) arrangement with gain enhancement. A TE/TM superimposing method was applied to derive the UC response over the entire area of the aperture of the TA based on the response analysis of a rotated UC satisfying 90° rotational symmetry to TE/TM oblique incidence. The designed TA antenna exhibits a low profile of F/D ratio = 0.33 at a center frequency of 3.5 GHz and a high aperture efficiency (AE) of 37%. The measured results are also in good agreement with the simulation results, indicating that the proposed TA antenna system provides an effective design methodology for SP array antennas and low-profile high-gain systems.**

***Index Terms*— Effective phase discontinuity (EPD), frequency-selective surface (FSS), low-profile high-gain system, slant polarization (SP), transmitarray (TA).**

I. Introduction

WIRELESS communication systems have advanced significantly in recent years due to considerable developments in antenna technologies. Particularly, transmitarray (TA) antennas that operate on a principle similar to that of lenses in optics have been of significant research interest, because they can manipulate the wavefront to achieve the desired behavior. TAs implemented in [1], [2], [3], [4], [5], [6], [7], [8], [9], [10], [11], [12], [13], [14], [15], [16], [17], [18], [19], [20], [21], [22], [23], [24], [25], [26], [27], and [28] have the advantages of being low-profile and lightweight, resulting in low fabrication cost, high efficiency, high gain, and enhanced beamforming.

The focal length-to-diameter (F/D) ratio, typically between 0.6 and 1.2 [8], affects the focal length, balancing radiation performance and aperture efficiency (AE). Many applications require TA systems with low height (low F/D) and high efficiency, regardless of the operating frequency. TA system height is determined by the TA thickness, the distance to the feeding antenna, and the feeding antenna's size. To achieve a low-profile design, two main strategies have been proposed: adjusting the feeding antenna's height or altering the spacing between the feeding antenna and the TA.

Most conventional TAs, such as those in [1], [5], [7], [10], [11], [13], [20], [23], and [24], use horn antennas for feeding due to their broadband radiation and high gain. However, horn antennas are inherently tall and have a high optimal F/D ratio (0.8–1.2) [5], making them unsuitable for low-profile applications. Although [5] reduced the profile by shortening the horn antenna and adding a frequency-selective surface (FSS), the system height remained substantial. In [7] and [12], a dipole with an FSS was used as the feeding antenna to lower the height, but this led to reduced system gain and efficiency. Moreover, the design process for an efficient low-profile feeding antenna was also not fully demonstrated.

Another approach involves reducing the system height by adjusting the spacing between the feeding antenna and the TA. This can be done by creating a virtual focal point using a folded TA (FTA) or by shortening the focal length with array feeding. The FTA method, as shown in [8], [9], uses a polarizer to achieve both reflection and transmission, reducing the focal length by 1/3 to 1/4. However, FTAs support only single polarization and typically suffer from low AE due to multiple reflections and transmissions. Xue et al. [14] addressed the short focal length issue by designing a unit cell (UC) with high angular stability. Despite this, there are no

Received 19 September 2023; revised 11 September 2024; accepted 9 October 2024. Date of publication 22 October 2024; date of current version 19 December 2024. This work was supported by the Samsung Global Technology Center (GTC). *(Corresponding author: Jungsuek Oh.)*

Uichan Park, Jinhyun Kim, Taeyeong Yoon, and Jungsuek Oh are with the Institute of New Media and Communication (INMC) and the Department of Electrical and Computer Engineering, Seoul National University, Seoul 08826, South Korea (e-mail: jungsuek@snu.ac.kr).

Haeseung Lee and Kyungho Yoo are with Global Technology Research, Samsung Electronics Company Ltd., Suwon 16677, South Korea.

Color versions of one or more figures in this article are available at https://doi.org/10.1109/TAP.2024.3481661.

Digital Object Identifier 10.1109/TAP.2024.3481661

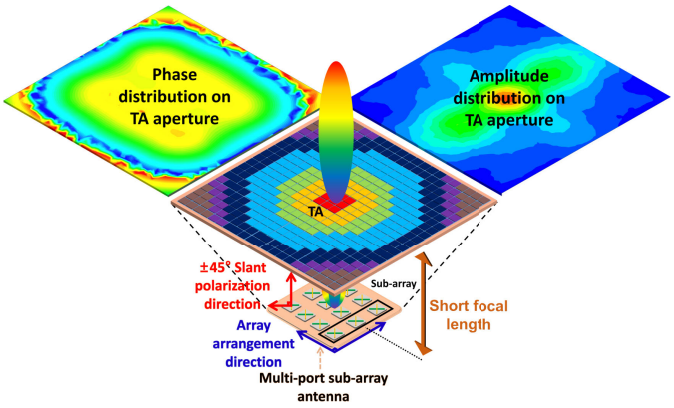

Fig. 1. Three-dimensional configuration of the proposed low-profile TA antenna system fed by MPSAs.

well-established techniques for achieving such stability beyond reducing cell size or maintaining the resonant length under oblique incidence. In addition, the use of horn antennas still results in significant system height.

In [15], an array feeding scheme was theoretically and numerically validated to operate at a lower focal length. Feng et al. [18] reported a TA with a Vivaldi array antenna for wideband operation at a low height. Aziz et al. [19] implemented a low-profile quad beam using slot array feeding. However, these designs are complex, requiring multiple feeding antennas, which increases design and implementation challenges. Moreover, the exact number of arrays needed was also not clarified.

Designing a compact, efficient TA system with a low focal length and reduced feeding antenna height is challenging and requires a co-design approach. Using an array antenna as the feeding source assumes ideal phase compensation, as discussed in [15], but achieving a short focal length introduces two main issues. First, the incident angle increases for UCs at the TA's edges, making it necessary to verify their performance under varying angles, which impacts overall efficiency. Second, as the F/D ratio decreases, significant phase variations occur across the TA aperture, leading to potential discrepancies in transmission response compared to infinite periodicity conditions. Reducing phase discontinuity by shrinking the unit cells is possible, but size reduction is limited by the wavelength.

This article introduces a new design for both the feeding antenna and the TA to overcome the limitations of previous designs. Multiport subarray antennas (MPSAs) with dual polarization (DP) arrays were employed to reduce both the focal length and the feeding antenna's height, as illustrated in Fig. 1. In addition, the TA was fed by a patch antenna with slant polarization (SP), which offers advantages such as uniform signal intensity and symmetric radiation patterns compared to vertical or horizontal polarization [29], [30], [31], [32].

We also explored increasing UC placement flexibility by rotating the cells, as opposed to the conventional arrangement method. The TE/TM oblique incidence effects on the rotated UC were analyzed mathematically, and the UC's response at various locations on the TA aperture was synthesized using the proposed TE/TM superimposing method. By calculating the mutual coupling coefficient between UCs based on polarization and applying the concept of effective phase discontinuity (EPD), we developed an efficient phase acquisition method for the TA system. This approach was used to analyze the oblique incidence and design the TA to minimize EPD. The height of the entire antenna system, including the feeding antenna and TA, is only 16.3 cm (1.89λ), making it sufficiently compact for low-profile applications. We also achieved an AE of 37% and an F/D ratio of 0.33 at 3.5 GHz.

The article is organized as follows: Section II-A describes the design process for the low-profile TA, while the MPSA feeding antenna is detailed in Section II-B. Section II-C presents the conventional UC design for TA, along with geometrical details and simulation results. The analysis of oblique incidence with TE and TM modes generated on the rotated UC is discussed in Section III-A. The TE/TM superimposing method and EPD are introduced in Sections III-B and III-C, respectively. Finally, simulation and measurement results are discussed in Section IV, with the conclusion provided in Section V.

II. Approach to Design a Low-Profile TA Antenna System

A. Overall Design Procedure for the Low-Profile TA Antenna

A design methodology for designing a low-profile TA antenna with a limited focal length for a specific application is outlined in Fig. 2. The flowchart is divided into three main parts: feeding antenna design, UC design, and TA design.

1) Feeding antenna design for low-focal length.
2) UC design.
3) TA design with an EPD analysis.

Before designing a low-profile TA system, key considerations include determining the desired operating frequency band, the total height of the feeding antennas, and the TA's focal length for the application. The number of feeding antennas is selected to achieve the optimal F/D ratio as suggested in [15].

The feeding antennas are designed to maximize the radiation efficiency at the operating frequency, and the dimensions of the TA with the maximum efficiency at a specific focal length are selected by analyzing the spillover efficiency and taper efficiency. If the desired gain is not met, the number of feeding antennas is adjusted.

Designing UCs requires ensuring they support the desired phase range and evaluating the impact of increased incident angles due to the low-profile design. Dey and Dey [33] and Venkatesh et al. [34] suggested that stable angular response can be achieved by reducing UC size and simplifying UC structure, but practical implementation remains challenging. This article presents an approach to enhance TA performance without requiring additional UC design modifications.

TA configuration involves optimizing UC arrangement based on reference phase changes. An iterative process is used to verify AE, incorporating a method to adjust unit arrangement using EPD after applying the proposed TE/TM superimposing method. This method is detailed in Section III-C.

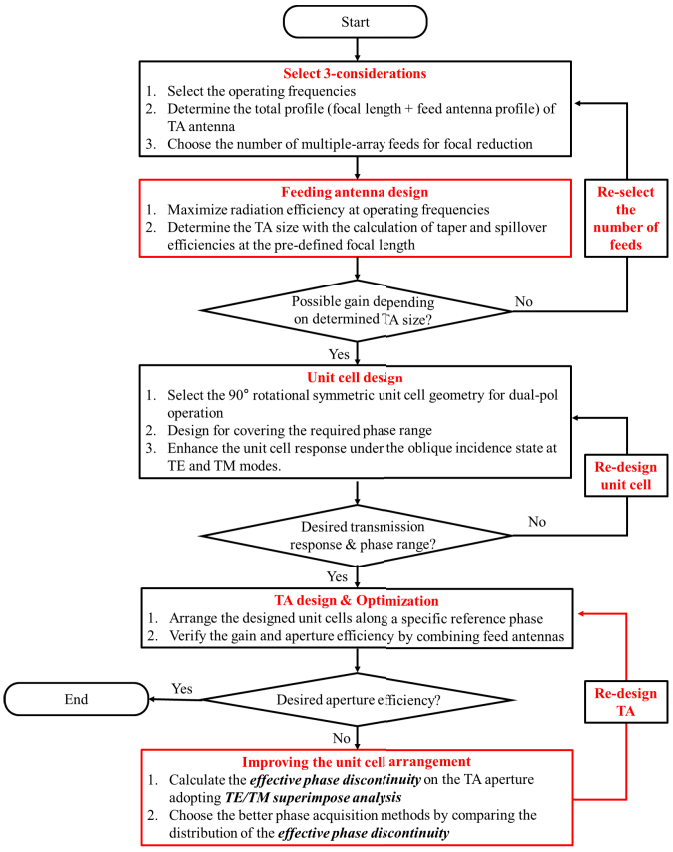

Fig. 2. Flowchart describing the process of designing an optimal dual-pol TA antenna that operates at a given profile.

Among the above design processes, this article describes the feeding antenna design and the TA size determination process to maximize efficiency, emphasizing additional methods to enhance TA performance logically.

B. Feeding Antenna Design With Multiport Subarray Configuration

Most commonly used feeding antennas in TA and FSS designs include dipole antennas, patch antennas, and horn antennas, each with inherent limitations. Dipole antennas offer low gain and lack broadband capability, while patch antennas are limited by their resonant structure. Horn antennas, despite their high gain and broad bandwidth, require significant length to maintain uniform phase and magnitude of the E-field across the radiating aperture, as discussed in [5]. This requirement increases the overall profile of the TA system, with an optimal F/D ratio typically ranging from 0.8 to 1.2.

To overcome these challenges, developing a novel feeding antenna is crucial. Clemente et al. [15] demonstrated that a low-profile TA can be achieved by reducing the focal length while maintaining radiation performance, provided that phase compensation on the TA aperture is precise. This study introduces an MPSA as a solution. The MPSA, consisting of multiple subarrays, simplifies the feed structure and facilitates the creation of a low-profile, high-efficiency TA antenna.

The TA's feeding antenna consists of four subarrays with a gain of approximately 11 dB, following the method in [15].

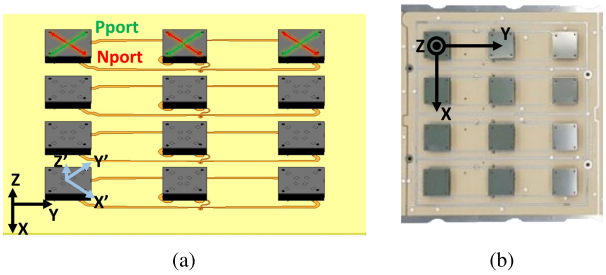

Fig. 3. Multiport antenna with subarray structure. (a) Three-dimensional model. (b) Fabricated antenna.

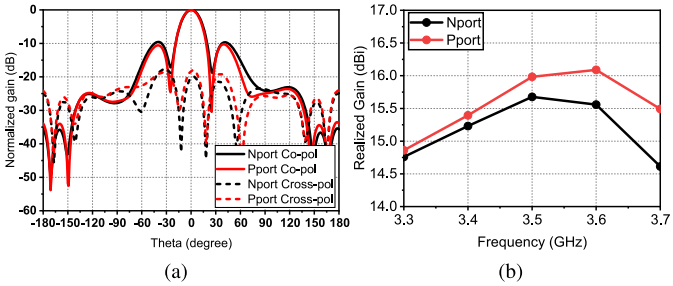

Fig. 4. Simulated radiation pattern and the realized gain level of the multiport antenna. (a) Radiation pattern at 3.5 GHz on the YZ-plane. (b) Gain level.

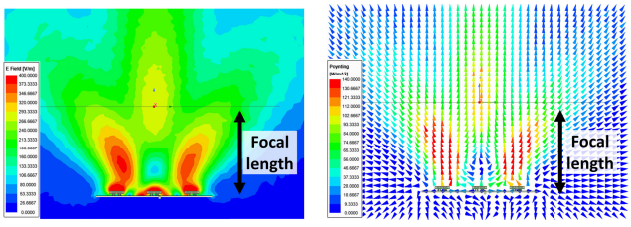

Fig. 5. (a) Complex magnitude of the radiating E-field of the MPSA. (b) Poynting vector plot.

Each subarray contains three patch antennas, utilizing a 3:1 divider to simplify the feeding network. Proper bandwidth is ensured using liquid crystal polymer (LCP) for indirect feeding. Fig. 3 shows the 3D model and fabricated MPSA with dual SP feeds on the N and P ports. The beam pattern and realized gain of the MPSA, depicted in Fig. 4, demonstrate a maximum gain of approximately 15–16 dB at 3.5 GHz in the boresight direction, with a 1-dB gain bandwidth spanning from 3.3 to 3.7 GHz, consistent with the TA's operating frequency.

Fig. 5(a) shows the E-field magnitude in the YZ-plane of Fig. 3, indicating that the radiated E-field intensity is highest at the side patches due to phase discrepancies between patches. This results in a different magnitude distribution compared to conventional single-fed antennas, characterized by two minor lobes. Given these characteristics of the MPSA, selecting the optimal focal length for both the feeding antenna and the TA is essential.

To achieve high AE in TA design, initial considerations should include spillover and taper efficiencies to determine the optimal focal length and TA dimensions. The spillover and taper efficiencies, as calculated using a full-wave simulator,

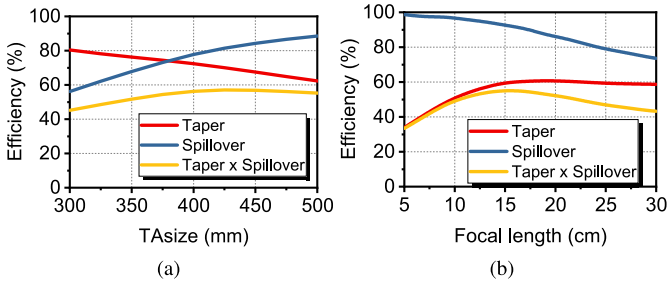

Fig. 6. Efficiency analysis under (a) TA size variation and (b) variation of focal length.

are expressed as follows [35]:

$$\eta_{taper} = \frac{1}{A}\frac{\left|\int\int_A I dA\right|^2}{\int\int_A |I|^2 dA} \tag{1}$$

$$\eta_{spillover} = \frac{\int\int_A \vec{S}\cdot d\vec{A}}{P_{rad}} \tag{2}$$

where I, A, S, and P_{rad} are the field intensity, surface of the TA, Poynting vector, and radiated power from the feeding antenna, respectively. Fig. 6 illustrates the results obtained from the full-wave simulator calculations for taper and spillover efficiencies, along with the feed efficiency multiplied by them.

Fig. 6(a) shows the efficiency as the TA size varies and (b) reveals the efficiency as the focal length variation. Once the required focal length of the system is determined (14 and 15 cm in this article), the optimal TA size should be determined through the previously designed MPSA, and it was determined to be 441 mm where the efficiency is maximized considering the UC size. Once the previously determined TA size is fixed and the efficiency analysis is performed according to the focal length, the result is shown in Fig. 6(b), and it can be seen that the highest efficiency is achieved at the predefined focal length.

It has a corresponding F/D of 0.33, which will eventually lead to an increase in incident angles and introduce phase distribution discontinuities on the aperture, as shown in Fig. 5(b). These discontinuities reduce the reliability of UC behavior based on the surrounded element approach [36], [37], disrupting phase compensation accuracy and altering magnitude response, ultimately decreasing TA efficiency. Therefore, to design a low-profile TA with high efficiency, the angular stability of the UC and the efficiency of UC placement on the TA aperture, leading to a phase-capturing method, must be carefully considered and analyzed.

C. UC Design

The aforementioned increase in the incident angle due to the decrease in F/D requires a UC design with high angular stability. However, designing such a UC is challenging, with no well-established theoretical methodology. Therefore, this study employs common FSSs, focusing on performance differences based on FSS arrangement.

Fig. 7 presents an exploded view of the UCs. Here, k_i represents the incident wave wavenumber, and ϕ_i denotes the

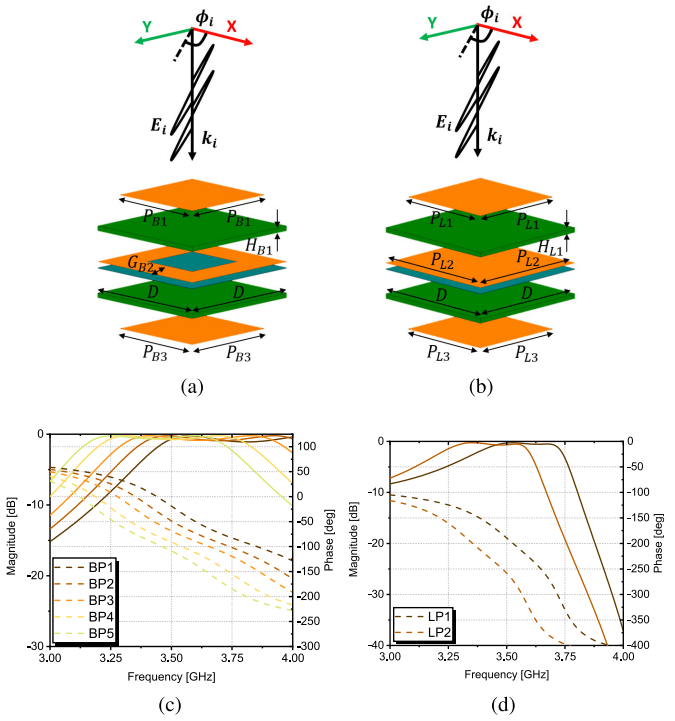

Fig. 7. Magnified view of the UCs. (a) Bandpass UC. (b) Lowpass UC, and magnitude and phase response of different UC types when $\phi_i = 0°$. (c) Bandpass UC. (d) Lowpass UC.

TABLE I
GEOMETRY PARAMETERS OF BANDPASS AND LOWPASS UCS

Parameters (mm)	P_{B1}/P_{L1}	G_{B2}/P_{L2}	P_{B3}/P_{L3}	D	H_{B1}/H_{L1}
BP1	17.3	7.5	17.3	21	1.52
BP2	17.8	7.5	17.8	21	1.52
BP3	18.2	7.5	18.2	21	1.52
BP4	18.7	7.5	18.7	21	1.52
BP5	19	7.5	19	21	1.52
LP1	19.6	20.6	19.6	21	1.52
LP2	20	20.7	20	21	1.52

angle between the E-field polarization direction and the UC. When $\phi_i = 0°$, the polarization direction is perpendicular to the patch edges in the UC. These UCs exhibit spatial bandpass and lowpass filter responses, as seen in [7]. A bandpass UC features a middle metal layer acting as a grid to form two complex poles [38], while a lowpass UC has limited high-frequency transmission due to the middle metal layer functioning as a patch. The desired phase range is achieved by adjusting the UC size. The normal incidence characteristics of the seven UCs used in the TA design are shown in Fig. 7(c) and (d), with corresponding UC dimensions in Table I.

Fig. 8 shows the UC response at oblique incidence for $\phi_i = 0°$. For the TE mode of the bandpass UC, increasing the incident angle raises the Q-factor, increasing passband insertion loss [39], as shown in Fig. 8(a). For the TM mode, a decreased Q-factor broadens the passband. Similar trends are observed in the lowpass UC response, where increased incident angles result in distinct insertion loss and phase compensation values compared to normal incidence. This implies that phase compensation accuracy diminishes, and loss increases toward the edge of the low-profile TA.

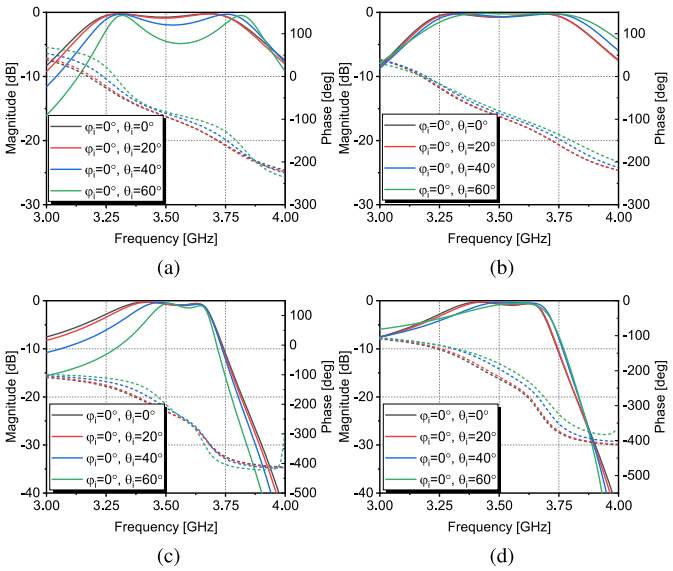

Fig. 8. Bandpass and lowpass UC response when $\phi_i = 0°$ with different incident angles. (a) Bandpass TE mode. (b) Bandpass TM mode. (c) Lowpass TE mode. (d) Lowpass TM mode.

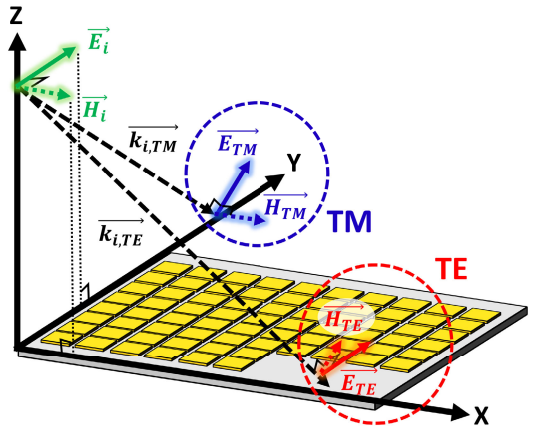

Fig. 9. Three-dimensional configuration with the oblique incidence of the TE and TM modes.

III. Novel UC Arrangement Method for TA Efficiency Improvement

Fig. 9 shows the generation of TE/TM modes on the XY-plane, with the E-field polarized in the y-direction. The TM mode lies in the YZ-plane, and the TE mode is in the XZ-plane. The wave vectors of these modes, $\overrightarrow{k_{i,TM}}$ and $\overrightarrow{k_{i,TE}}$, are perpendicular to both the E- and H-fields. When the UCs are placed at the aperture of the TA, TE/TM modes form based on polarization, leading to oblique incidence depending on the UC's position. Thus, evaluating the TE/TM mode responses under varying incident angles is crucial when designing a low-profile TA.

For the ±45° SP feed array antenna in Fig. 3, the array arrangement direction is misaligned with the polarization direction. This necessitates analyzing the TE/TM mode responses in a rotated UC (i.e., $\phi_i \neq 0°$). Specifically, the following sequence should be followed:

1) Evaluate TE/TM modes for oblique incidence with $\phi_i = 0°$ and $\theta \neq 0°$.

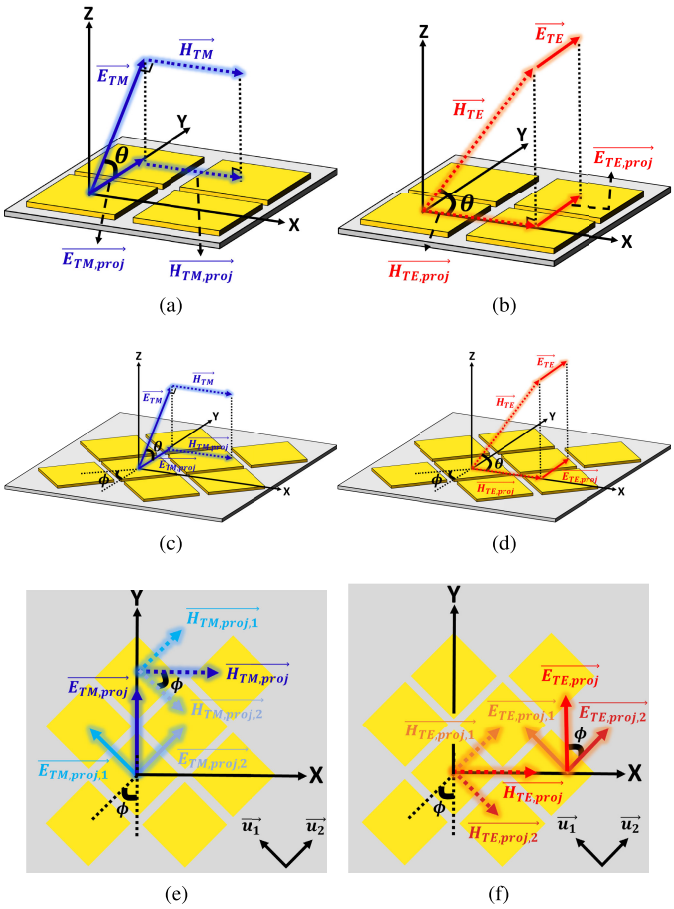

Fig. 10. Vector expression of E- and H-fields of the TE and TM waves under different UC arrangements which are perpendicular to x- and y-axes with the (a) TM mode and (b) TE mode; rotated by ϕ on the z-axis with the (c) TM mode, (d) TE mode, (e) top view of the TM mode, and (f) top view of the TE mode.

2) Evaluate TE/TM modes for oblique incidence with $\phi_i \neq 0°$ and $\theta \neq 0°$.

This approach enables effective analysis of TE/TM modes as the UC rotates relative to the polarization direction, and when incident waves propagate at an oblique angle. Section III-A will validate the considerations outlined above.

A. Floquet Response Characteristics of the TE and TM Modes Oblique Incident on the Rotated UCs

E and H vectors for the TM and TE regions on the TA aperture depending on the UC arrangement method are shown in Fig. 10. The wave impedance for a unit-cell arrangement perpendicular to the x- and y-axes (common method) can be calculated with Fig. 10(a) and (b). The wave impedance of the oblique incidence is expressed as [39]

$$\eta_{TM,\theta} = \frac{\left|\overrightarrow{E_{TM,proj}}\right|}{\left|\overrightarrow{H_{TM,proj}}\right|} = \frac{\left|\overrightarrow{E_{TM}}\right|}{\left|\overrightarrow{H_{TM}}\right|} \times cos\theta = \eta_o \times cos\theta \quad (3)$$

$$\eta_{TE,\theta} = \frac{\left|\overrightarrow{E_{TE,proj}}\right|}{\left|\overrightarrow{H_{TE,proj}}\right|} = \frac{\left|\overrightarrow{E_{TE}}\right|}{\left|\overrightarrow{H_{TE}}\right|} \div cos\theta = \eta_o \div cos\theta \quad (4)$$

where η_o is the wave impedance in free space. By comparing the magnitudes of the E and H waves projected onto the plane where the UC is placed as described in [39], the TE and TM mode responses for a specific region can be predicted.

Fig. 10(c) and (d) illustrates the E- and H-field vectors for the TM and TE modes when the UC is rotated by ϕ around the z-axis. These fields, projected onto the XY-plane, are decomposed along the UC's directional unit vectors $\overrightarrow{u_1}$ and $\overrightarrow{u_2}$. The wave impedance in the case of rotated UC for the TM mode is derived with vector decomposition as follows:

$$\eta_{TM,\theta,1} = \frac{\left|\overrightarrow{E_{TM,proj,1}}\right|}{\left|\overrightarrow{H_{TM,proj,1}}\right|} = \frac{\left|\overrightarrow{E_{TM,proj}} sin\phi\right|}{\left|\overrightarrow{H_{TM,proj}} sin\phi\right|} = \frac{\left|\overrightarrow{E_{TM}}\right|}{\left|\overrightarrow{H_{TM}}\right|} cos\theta = \eta_o cos\theta \tag{5}$$

$$\eta_{TM,\theta,2} = \frac{\left|\overrightarrow{E_{TM,proj,2}}\right|}{\left|\overrightarrow{H_{TM,proj,2}}\right|} = \frac{\left|\overrightarrow{E_{TM,proj}} cos\phi\right|}{\left|\overrightarrow{H_{TM,proj}} cos\phi\right|} = \frac{\left|\overrightarrow{E_{TM}}\right|}{\left|\overrightarrow{H_{TM}}\right|} cos\theta = \eta_o cos\theta. \tag{6}$$

In the case of the TE mode, the wave impedance on the rotated UC is obtained by applying the same method as in the TM mode analysis

$$\eta_{TE,\theta,1} = \eta_{TE,\theta,2} = \frac{\left|\overrightarrow{E_{TM}}\right|}{\left|\overrightarrow{H_{TM}}\right|} \div cos\theta = \eta_o / cos\theta. \tag{7}$$

Equations (5)–(7) imply that the UC is rotationally arranged irrespective of the angle ϕ, and the wave impedance is the same as that in the conventional TM and TE responses incident at an angle of θ.

Fig. 11 compares the bandpass and lowpass UC responses for varying ϕ_i and θ_i. The results confirm that TE/TM responses are independent of UC rotation for UCs with 90° rotational symmetry as previously demonstrated in (3)–(7), offering additional flexibility in UC arrangement.

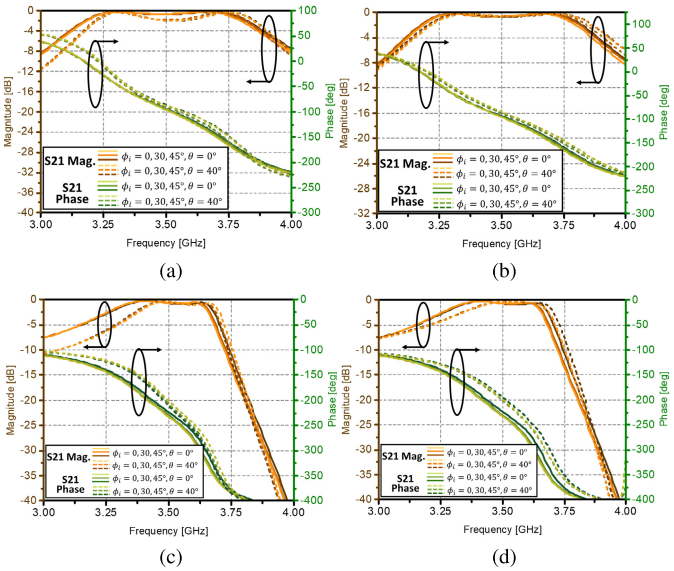

Fig. 11. Bandpass and lowpass UC magnitude and phase response with different incident angles (θ_i) and UC rotation angles (ϕ_i). (a) Bandpass TE mode. (b) Bandpass TM mode. (c) Lowpass TE mode. (d) Lowpass TM mode.

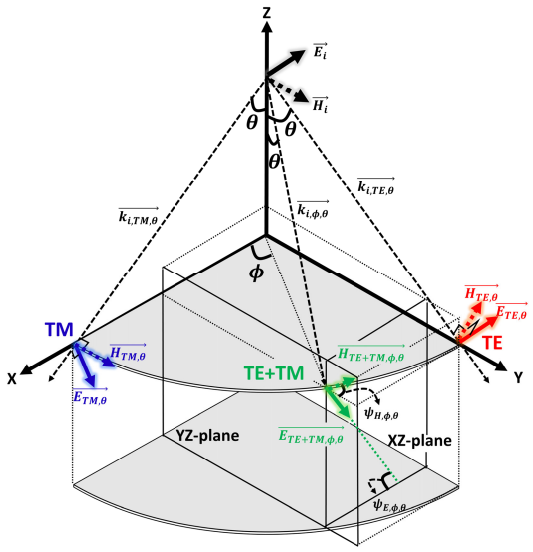

Fig. 12. Three-dimensional configuration of the region where TE, TM, and TE + TM combined modes are synthesized on the arbitrary point of the TA aperture plane.

B. UC Response Derivation of the TE/TM Modes Overlapped Region

The TA design for a particular feeding antenna requires consideration of the phase and magnitude distribution of the E-field formed on the TA aperture, as well as the analysis of the TM and TE modes on the TA aperture. The E-field propagating from the feeding antenna not only forms the TM and TE modes but also forms a superposition of the TM and TE modes as shown in Fig. 12. Assuming that the feeding antenna is a point source, the angle formed between the wave vector of the incident wave on the UC and the z-axis is defined as θ. The UC response in the region where the TM and TE modes overlap can be represented as follows by synthesizing the TM and TE responses with an incident angle of θ

$$S_{\phi,\theta,TE+TM} = A * S_{\theta,TM} + B * S_{\theta,TE}. \tag{8}$$

A and B in (8) are the weights of the TM and TE responses of a UC with an incident angle of θ, respectively. They can be calculated by utilizing the property that the wave vector of the feeding source and the E- and H-fields formed on a particular aperture are perpendicular to each other.

From Fig. 12, the E- and H-fields of TM and TE modes at the TA aperture can be defined by the following equation.

$$\overrightarrow{E_{TM,\theta}} = \langle -cos\theta, 0, -sin\theta \rangle, \quad \overrightarrow{E_{TE,\theta}} = \langle -1, 0, 0 \rangle$$
$$\overrightarrow{H_{TM,\theta}} = \langle 0, 1, 0 \rangle, \quad \overrightarrow{H_{TE,\theta}} = \langle 0, cos\theta, sin\theta \rangle. \tag{9}$$

In addition, the wave vector propagating into the region where the TM and TE modes are superimposed is

$$\overrightarrow{k_{i,\phi,\theta}} = \langle sin\theta cos\phi, sin\theta sin\phi, -cos\theta \rangle. \tag{10}$$

Moreover, the E- and H-fields formed in the superimposed region can be expressed as follows:

$$\begin{aligned}\overrightarrow{E_{TE+TM,\phi,\theta}} &= \langle -cos\psi_E, 0, -sin\psi_E\rangle \\ \overrightarrow{H_{TE+TM,\phi,\theta}} &= \langle 0, cos\psi_H, sin\psi_H\rangle. \end{aligned} \tag{11}$$

As the polarization of the feeding antenna is in the x-axis direction, the E-field in the superposed area lies in the XZ-plane, and the H-field lies in the YZ-plane. Furthermore, the wave vector and electromagnetic field vectors must always be perpendicular. Thus

$$\begin{aligned}\overrightarrow{k_{i,\phi,\theta}} \cdot \overrightarrow{E_{TE+TM,\phi,\theta}} &= 0 \\ \overrightarrow{k_{i,\phi,\theta}} \cdot \overrightarrow{H_{TE+TM,\phi,\theta}} &= 0 \end{aligned} \tag{12}$$

can be obtained. Expanding using (11) and (12), we obtain ψ_E and ψ_H, which are related to the directional vectors of the E- and H-fields in the region where the TM and TE modes are overlapped, as follows:

$$\begin{aligned} tan\psi_E &= tan\theta cos\phi \\ tan\psi_H &= tan\theta sin\phi. \end{aligned} \tag{13}$$

In practice, if the TA diameter is 441 mm and the focal length is 145 mm, as is the situation in the present paper, ψ_E and ψ_H at the edges of the TA at $\phi = 45°$ will be 56.7°. This represents a substantial angle of incidence.

In addition, the E-field vector $\overrightarrow{E_{TE+TM,\phi,\theta}}$ in the region where TM and TE modes are superimposed can be expressed as the E-field vector $\overrightarrow{E_{TM,\theta}}$ in the TM region and the E-field vector $\overrightarrow{E_{TE,\theta}}$ in the TE region as follows:

$$\begin{aligned} A_E * \overrightarrow{E_{TM,\theta}} + B_E * \overrightarrow{E_{TE,\theta}} &= \overrightarrow{E_{TE+TM,\phi,\theta}} \\ A_H * \overrightarrow{H_{TM,\theta}} + B_H * \overrightarrow{H_{TE,\theta}} &= \overrightarrow{H_{TE+TM,\phi,\theta}} \end{aligned} \tag{14}$$

so are the H-fields. A and B represent the weights of the TM and TE regions response, respectively, which can be summarized as follows using (9), (11), and (13)

$$\begin{aligned} A_E &= \frac{sin\psi_E}{sin\theta}, \quad B_E = \frac{sin(\theta - \psi_E)}{sin\theta} \\ A_H &= \frac{sin(\theta - \psi_H)}{sin\theta}, \quad B_H = \frac{sin\psi_H}{sin\theta}. \end{aligned} \tag{15}$$

Consequently, the E and H fields in the TM and TE modes overlapped regions can be synthesized based on the E and H fields of the TM mode and TE mode using the above method. Furthermore, as described in Section III-A, regardless of whether the UC array satisfying 90° rotational symmetry is rotated or not, the UC response in the region where the two modes overlap can be synthesized; conversely, this cannot be obtained by conventional Floquet simulation. The proposed method makes it possible to extract the response in the region where the TM and TE modes of a UC incident at a certain angle (i.e., θ) and rotated by a certain angle (i.e., ϕ) are synthesized. This will be discussed in more detail in Section III-C.

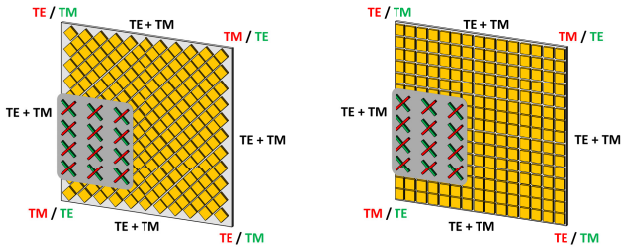

Fig. 13. Conceptual graphical diagram of the UC arrangement of the low-profile TA antenna for MPSA feeding antenna. (a) Type 1: Arrangement of UCs parallel to the direction of polarization. (b) Type 2: Arrangement of UCs at a 45° tilt to the direction of polarization.

C. Low-Profile Transmitarray Antenna Design Considering EPD

As demonstrated in Section III-A, the response of the UC is independent of its rotational arrangement. Based on this, the TA can be constructed using various UC placement methods, as shown in Fig. 13. Two configurations are illustrated: Type 1, where the polarization and UC arrangement directions are aligned [Fig. 13(a)], and Type 2, where they are rotated by 45° [Fig. 13(b)]. Both configurations maintain the same aperture size and reference phase, allowing a direct comparison of their performance. As will be shown, Type 2 achieves superior phase compensation and higher gain, as verified through simulations. To evaluate the UC arrangement efficiency, scattering matrix coefficients representing mutual coupling between UCs along the polarization and UC arrangement directions must be extracted. These coefficients, denoted as S_{mn}, are defined by [40]

$$\begin{aligned} S_{mn} = \frac{1}{4\pi^2}\int_{-\pi}^{\pi}\int_{-\pi}^{\pi} S^{FL}(\psi_x, \psi_y) \\ \times exp\left[j\left(\frac{d_x\psi_x}{a} + \frac{d_y\psi_y}{b}\right)\right] d\psi_x d\psi_y \end{aligned} \tag{16}$$

where a and b are the element spacings along the x- and y-directions, respectively; ψ_x and ψ_y are the phase differences between the adjacent elements along the x- and y-directions, respectively; d_x and d_y are the relative coordinates of the mth element along the x-axis and nth element along the y-axis, respectively; and S^{FL} is the s-parameter of an array element under Floquet simulation.

To extract the mutual coupling coefficients between the UCs, the S-parameter responses for TM and TE modes generated by different incident angles under Floquet simulation conditions are required. Fig. 14 shows the simulation setup utilizing HFSS to extract the UC responses under Floquet mode conditions. The Floquet response of the UC under TM and TE modes can be extracted by varying the incident angle. Simulations performed for $\phi = 0°$ and $\phi = 45°$ confirm that the UC response remains independent of ϕ for UCs with 90° rotational symmetry. Thus, S^{FL} applies equally regardless of ϕ, and only the phase differences ψ_x and ψ_y vary with polarization rotation.

Fig. 15 defines ψ_x and ψ_y for TM and TE modes in the TA aperture, where $\psi_x = k_0 asin\theta cos\phi$ and $\psi_y = k_0 bsin\theta sin\phi$. a and b are equal to the spacing between the UC,

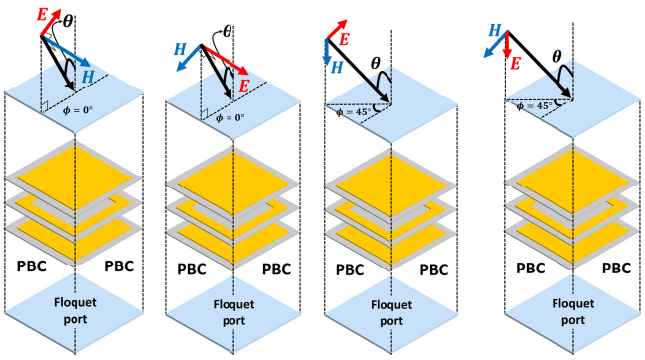

Fig. 14. Floquet simulation setup of the UC with periodic boundary conditions with different ϕ. (a) TM mode when $\phi = 0°$. (b) TE mode when $\phi = 0°$. (c) TM mode when $\phi = 45°$. (d) TE mode when $\phi = 45°$.

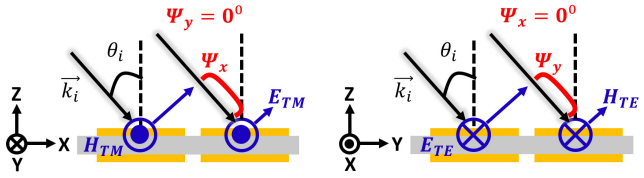

Fig. 15. Illustration of the phase difference between UCs due to oblique incidence of TM and TE waves. (a) TM mode. (b) TE wave.

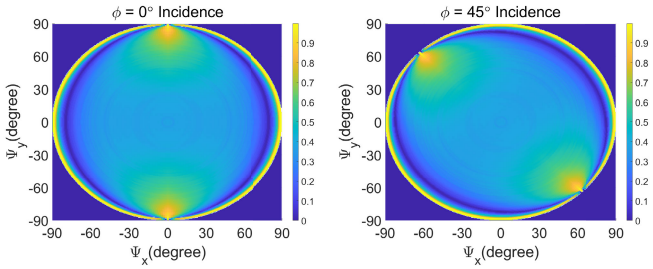

Fig. 16. Bandpass UC magnitude response of the reflection coefficient as a function of the phase difference between the UCs due to oblique incidence. (a) $\phi = 0°$. (b) $\phi = 45°$.

particularly, 21 mm in this case. For TM modes along the x-axis, ψ_x reaches its maximum, while ψ_y is minimized, and vice versa for TE modes. Response on mixed regions of the TM and TE modes is essential to calculate the mutual coupling, which cannot be obtained in the conventional Floquet simulation setup. Instead, the TM/TE decomposition and synthesis scheme analyzed and presented in Section III-B can be used to derive the response on mixed regions of the TM and TE modes.

Fig. 16 shows the bandpass UC's magnitude response of the reflection coefficient as a function of ψ_x and ψ_y, which vary with the incident angle. The response for the overlapping TM and TE modes is also shown. Fig. 16(a) reveals the magnitude response of the reflection coefficient when $\phi = 0°$. When $\psi_y = 0$, the magnitude of the reflection coefficient decreases as ψ_x increases. When $\psi_x = 0$, the response of the TM region can be seen. Fig. 16(b) shows the reflection coefficient magnitude response when $\phi = 45°$. The reflection

-42.1	-28.9	-26.8	-28.9	-42.1
-18.0	-15.1	-14.7	-15.1	-18.0
-14.4	-12.2	-12.0	-12.2	-14.4
-18.0	-15.1	-14.7	-15.1	-18.0
-42.1	-28.9	-26.8	-28.9	-42.1

(a)

-28.5	-31.9	-19.5	-16.7	-20.3
-31.9	-17.9	-13.4	-12.7	-16.7
-19.5	-13.4	-11.9	-13.4	-19.5
-16.7	-12.7	-13.4	-17.9	-31.9
-20.3	-16.7	-19.5	-31.9	-28.5

(b)

Fig. 17. Mutual coupling (S_{ij}) between the center element and other elements of a UC array in an infinite array environment. (a) $\phi = 0°$, Type 1. (b) $\phi = 45°$, Type 2.

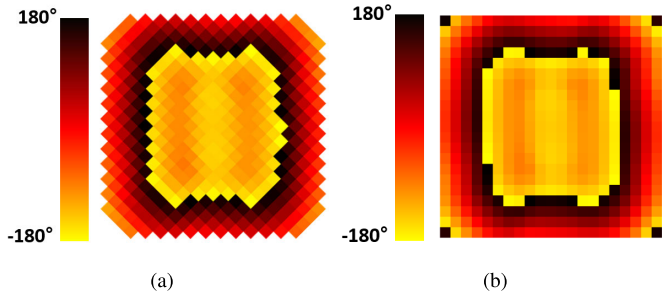

Fig. 18. Phase distribution for different phase acquisition methods. (a) Phase acquisition in parallel with the direction of polarization: Type 1. (b) Phase acquisition with a 45° tilt to the direction of polarization: Type 2.

coefficient magnitude response varies with ψ_x and ψ_y as the polarization direction is changed. From the derived reflection coefficient response, the mutual coupling coefficient of Type 1 and Type 2 TA can be calculated.

The mutual coupling coefficients can be obtained from (16), which is shown in Fig. 17. The values indicate mutual coupling in decibels of the respective element with the center (orange) element. In addition, the yellow-colored cells indicate the direction of the polarization. The magnitude of the mutual coupling coefficient between the UCs listed in the direction of the polarization is higher, as can be seen from the table.

Fig. 18 presents the phase distribution for the UCs in both Type 1 and Type 2 configurations. The two-phase distributions are obtained from the phase of the E field formed on the TA aperture and have the same reference phase. From the phase distributions formed by the different phase acquisition methods, the EPD ($\Delta\Phi_{m,n,eff}$) between the neighboring adjacent UCs can be shown as follows:

$$\Delta\Phi_{m,n,eff} = \frac{1}{N} \sum_{\Delta x \in A_m, \Delta y \in A_n} S_{\Delta x,\Delta y} \left| \Phi_{m,n} - \Phi_{m+\Delta x, n+\Delta y} \right|$$
$$s.t.\ A_m = \{\Delta x | \Delta x \in \{-1, 0, 1\}, m + \Delta x > 0\}$$
$$A_n = \{\Delta y | \Delta y \in \{-1, 0, 1\}, n + \Delta y > 0\} \quad (17)$$

where $\Phi_{m,n}$ is the phase of the E field on the mth and nth elements, $S_{\Delta x,\Delta y}$ is the mutual coupling coefficient derived from (16), Δx and Δy indicate the moving index of the neighboring UCs compared to the reference UC on the x- and y-axes, respectively, and N is the number of the neighboring UCs.

The EPD between the UCs lying on the TA aperture can be calculated as the average of the actual phase difference

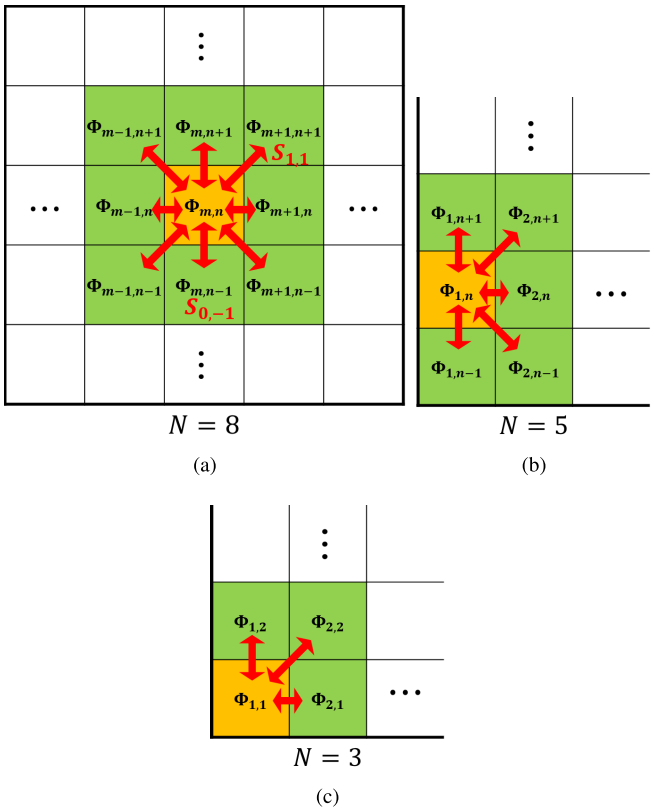

Fig. 19. Schematic of the calculation of the number of neighboring UCs and EPD, which varies with the position of the reference UC on the TA aperture. (a) State when the reference UC is in the center region and has eight neighboring UCs. (b) State when reference UC is attached to one side and has five neighboring UCs. (c) State when reference UC is attached to two sides and has three neighboring UCs.

between the reference UC and neighboring UCs multiplied by the magnitudes of the mutual coupling coefficients as weight factors. Fig. 19 shows the number of neighboring UCs as a function of the position of the reference UC on the TA aperture. For example, if the reference UC touches two sides of the TA, as shown in Fig. 19(c), the EPD can be calculated as follows:

$$\Delta\Phi_{1,1,eff} = \frac{1}{3}|S_{0,1}||\Phi_{1,1} - \Phi_{1,2}| + \frac{1}{3}|S_{1,1}||\Phi_{1,1} - \Phi_{2,2}| + \frac{1}{3}|S_{1,0}||\Phi_{1,1} - \Phi_{2,1}|. \quad (18)$$

In the same manner, the EPD can be calculated for phases formed on the apertures Types 1 and 2 with different UC arrangements. Fig. 20 shows the calculated EPD for the two TA configurations. The larger the EPD between neighboring UCs, the redder it is; the smaller values are indicated in blue color. Both types of TAs exhibit a small EPD in the center of the aperture where the radiated power is concentrated, and the EPD increases toward the edge of the aperture. Fig. 20(b) indicates that the Type 2 TA has a larger area of small EPD in the center of the aperture than that in the Type 1 TA. Furthermore, the Type 2 TA exhibits a lower EPD toward the edge of the aperture. This means that the phase acquisition method and the UC arrangement method of Type 2 have a lower phase change rate than that of Type 1 at a given aperture.

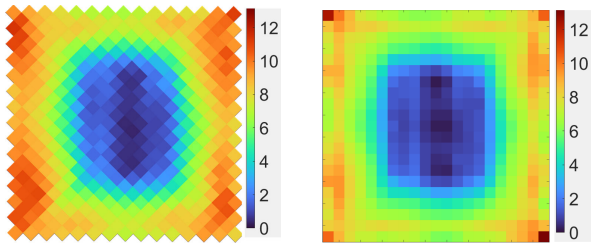

Fig. 20. Distribution of effective phase discontinuities between a reference cell and its neighbors, weighted by the mutual coupling coefficients for different phase acquisition methods. (a) Phase acquisition in parallel with the direction of polarization: Type 1. (b) Phase acquisition with a 45° tilt to the direction of polarization: Type 2.

It leads to a smaller dimensional difference between UCs arranged concerning a specific phase.

As a method to check the accuracy and approximation of the UC simulation, the surrounded element approach [36], [37] is used. In most UC simulations, the S-parameter response is verified under the infinite periodic structure condition. However, in the case of UCs placed in an actual TA design, there will be geometric and dimensional differences between UCs. The larger the geometric difference between the reference UC and the surroundings, the greater will be the difference from the response of the infinite periodic structure. In addition, it leads to inaccurate phase compensation or large insertion losses [20]. The smaller the effective phase change, the fewer will be structural differences between the placing UCs, resulting in a more stable phase and magnitude response. Hence, the phase acquisition method of the Type 2 TA has a more efficient phase compensation and higher gain than that in Type 1 TA.

IV. Simulation and Experimental Results of TA

A. Simulation Results

Fig. 21 shows the simulated normalized radiation pattern for the Type 2 TA at different frequencies and SP angles (−45° and +45°). At the center frequency of 3.5 GHz, the sharp beam pattern indicates effective phase compensation, with both polarizations showing sidelobe levels (SLL) below −20 dB. The cross-polarization level at boresight is about −25 dB, demonstrating good polarization separation.

At the 3.3- and 3.7-GHz operating frequencies, which is the operating range of the 1-dB gain BW of the feeding antenna, it can be seen that the SLL is about −15 to −18 dB as shown in Fig. 21(a), (b), (e), and (f), which is a result of the change in phase distribution with the change in the operating frequency of the feeding antenna and the bandwidth limitation of the UC. The polarization level is worse than the center frequency band but still remains at or below −18 dB.

Fig. 22 compares the simulated and measured results for different types of TA as a function of frequency and polarization. For the Type 2 TA, which has a high gain as demonstrated by the EPD, the realized gain is 21.3 and 20.6 dB in the simulation results for N-port and P-port polarizations, respectively, at 3.5 GHz. In contrast, the Type 1 TA presented realized gains of 19.1 and 19.5 dB, respectively, at 3.5 GHz. Type 2 TA has

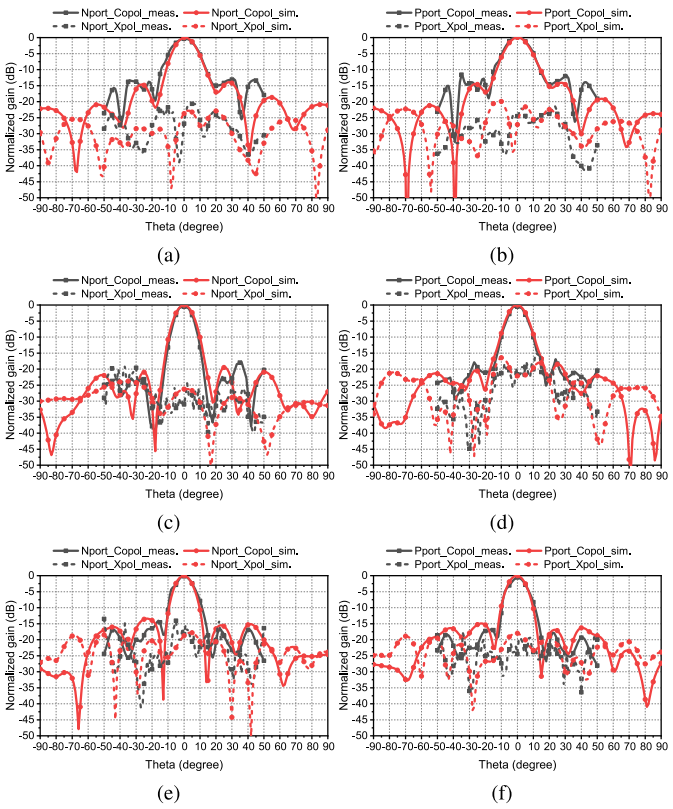

Fig. 21. Simulated and measured normalized radiation patterns in the YZ-plane of the Type 2 TA antenna on 3.3 GHz: (a) N port and (b) P port; 3.5 GHz: (c) N port and (d) P port; 3.7 GHz: (e) N port and (f) P port.

TABLE II
LOSS BUDGET OF THE DESIGNED TA AT CENTER FREQUENCY

Ideal directivity	25.14 dB
Return loss	0.2 dB
Spillover loss	0.33 dB
Taper loss	2.24 dB
TA insertion loss	0.5 dB
Dielectric and conductive losses	0.6 dB
Realized gain	21.3 dB

a gain that is between 1 and 2 dB higher than Type 1 TA. Realized gain can be converted to AE, which can be calculated as follows:

$$A_{eff} = \frac{\lambda^2}{4\pi} G_{obtained}$$
$$\eta_{ap} = \frac{A_{eff}}{A_{physical}} \tag{19}$$

where $A_{physical}$ is the physical area of the TA, and $G_{obtained}$ is the realized gain. For Type 2 TA, the N-port polarization has an AE of 40.6%, compared to 24.4% for Type 1 TA, indicating a 16% improvement due to enhanced phase acquisition and UC placement. Table II shows the loss budget of the proposed Type 2 TA. Spillover and taper loss were calculated in Section II-B. In addition, dielectric and conductive losses denote the loss of the feeding antenna, showing a radiation efficiency of 88%. Eventually, for the total low-profile TA system combined, 79% radiation efficiency was obtained.

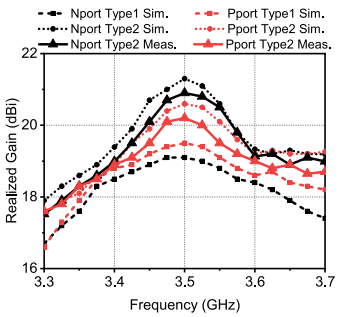

Fig. 22. Simulated and measured realized gain level with the frequency of the different TA antenna types.

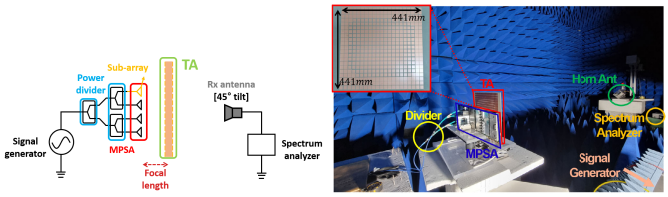

Fig. 23. Conceptual diagram and measurement setup for the measurement of the TA. (a) TA antenna measurement diagram and (b) practical implementation of the measurement setup.

One factor to note is that gain improvement diminishes at 3.3 and 3.7 GHz compared to the center frequency. Fig. 7 shows that while certain UCs exhibit good insertion loss at 3.5 GHz, UCs at 3.3 and 3.7 GHz have insertion losses of up to −5 and −10 dB, respectively, which reduces the effective phase distribution (EPD). This results in signal attenuation through the UC, limiting gain improvement at these frequencies. The bandwidth of the UC affects the frequency range over which gain increases, so a wider-band UC design would yield a broader gain improvement.

B. Experimental Results

The fabricated Type 2 TA consists of three metal layers (35-μm thick) and two TLF-35 substrates (1.52-mm high), with a total thickness of 3.04 mm. The aperture is 441 × 441 mm^2, comprising 441 UCs, each 21 cm in size. The distance between the TA and the feeding antenna is 14 cm, corresponding to an F/D ratio of 0.33.

Fig. 23 shows the measurement setup using a signal generator and spectrum analyzer to measure the fabricated TA. The signal generator side utilizes three dividers for MPSA in-phase feeding with four subarrays, and the spectrum analyzer side uses a reference horn antenna with predefined gain. To measure the absolute gain of the TA and MPSA, the path loss (i.e., Thru) calibration process is performed using two horn antennas with known gain, and after compensating for the loss component of the used divider, the feeding antennas MPSA and TA are placed to measure the absolute gain.

The measured beam pattern of the proposed TA using the aforementioned measurement setup is shown in Fig. 21. Due to the long wavelength of the 3.5-GHz band and the large physical size of the feeder and TA, only YZ-plane measurements could be performed. In addition, rotation of the

TABLE III
COMPARISON WITH OTHER TA ANTENNAS

Ref.	Frequency (GHz)	F/D	AE (%)	Size ($\lambda_o \times \lambda_o$)	Thickness (λ_o)	Measured max gain (dBi)	UC type	1dB gain BW (%)	Total system height (λ_0)	Antenna type	Polarization
[3]	13.3	0.75	37.9	5x5	0.07	21.3	FSS & Patch	7.5	3.82+H_s[5)]	Horn TA	Single
	13.3	0.75	29.3	10x10	0.07	26.2	FSS & Patch	6.7	7.57+H_s	Horn TA	Single
[4]	28	0.5	24.5	9.45[2)]	0.18	24.2	Metamaterial	7.1[4)]	5.79	Patch TA	Single
[5]	100	-	46	7.6x5.7	0.042	23.8	FSS	-	6.67	Horn TA	Single
[7]	28	0.7	7	4.8[2)]	0.05	12	FSS	5.4[4)]	3.41	Dipole TA	Single
[8]	29	0.3[1)]	12.6	16[2)]	0.1	24.7	Polarizer	8.62[4)]	4.6+H_s[5)]	Horn FTA	Single
[9]	27	0.29[1)]	44.7	7.2[2)]	0.04	24	Polarizer	25.9	3.8	Horn FTA	Single
[12]	1.95	0.53	26.3[3)]	2.6x2.6	0.4	13.5	FSS	-	2.03	Dipole TA	Single
[14]	28	0.32	40.3	15x15	0.14	30.6	Huygens	7.14[4)]	4.94+H_s[5)]	Horn TA	Single
[19]	12.4	0.05	42.5	18.8x18.8	0.76	26.5	FSS	5.24	1.66+H_s[5)]	Slot array TA	Single
Proposed	3.5	0.33	37	5.1x5.1	0.035	20.9	FSS	5.7	1.89	Multi patch TA	Dual

[1)] H/D (FTA) [2)] Diameter of a circular array [3)] Value inferred from the graph [4)] Calculated from the graph [5)] Height of the feeding source

DUT antenna is required to measure the beam pattern, and because of the rotation angle limitations of the rotation table where the TA and MPSA are placed, beam patterns from −50° to 50° were measured.

In Fig. 21(c), the N port polarization exhibits the highest gain at 3.5 GHz, with an HPBW of about 10° and the highest SLL of about −17 dB. The cross-polarization level also remains low, below −20 dB at boresight. The 3.3- and 3.7-GHz cases show HPBWs of about 18° and 14°, respectively, and both show low SLLs below −15 dB and low cross-polarization levels below −20 dB. Fig. 21(b), (d), and (f) displays the results of the P port polarization, which again shows the highest gain at 3.5 GHz. Overall, it exhibits a similar radiation pattern to the N port and has an HPBW of about 12°. The 3.3- and 3.7-GHz bands also exhibit SLLs below −14 dB and cross-polarization levels below −17 dB.

The measured realized gain for the Type 2 TA with a short dashed line is depicted in Fig. 22. At the center frequency of 3.5 GHz, the N-port and P-port gains are measured to be 20.9 and 20.2 dB, respectively, a reduction of 0.4 dB from the simulation. AE can be calculated to 37% and 31.5% from the measured data. At 3.3 and 3.7 GHz, gains of 17.5 and 18.8 dB were measured, aligning closely with simulated values. Thus, by acquiring the phase of the feeding antenna at a 45° tilt to the direction of polarization, we were able to experimentally verify a TA that exhibits the same high gain as the simulation in a low profile.

Table III summarizes the performance of the recent works on TA antenna systems. As shown in the table, the proposed TA antenna supporting dual SP exhibits a low F/D, resulting in a low-profile system with an extremely low total height of $1.89\lambda_0$, while maintaining a high AE of 37%. The low bandwidth is caused by the bandwidth limitation of the FSS UC and the nonuniformity of the gain of the MPSA used as the feeding antenna, but it shows a very low thickness by utilizing the FSS implementation with two substrates.

V. CONCLUSION

This article presents a low-profile TA system that utilizes MPSA feeding with SP and introduces the concept of EPD on the aperture surface, which is experimentally verified. The proposed TA has advantages over novel UC arrangements that do not match the polarization direction. By analyzing the response of polarization not incident perpendicular to the sides of a UC satisfying 90° rotational symmetry, verifying the TM/TE oblique incidence, and deriving the response to the region where the two modes overlap, we increased the degrees of freedom of the phase acquisition method. The presented TA realizes a high AE of approximately 37% at a low F/D ratio of 0.33, achieving an efficient low-profile system of feeding and TA antenna. Dual-polarization operation and high gains up to 21.3 and 20.6 dB are achieved at an operating frequency of 3.5 GHz. The proposed TA antenna system and its analysis with design procedure will contribute to efficient miniaturization and high gain realization of an array antenna system operating at not only sub-6 GHz but also at other frequencies.

REFERENCES

[1] J. Kim, J. Kim, J. H. Oh, S.-H. Wi, and J. Oh, "Rotated feed-combined reconfigurable transmit RIS with disparate deployment of 1-bit hybrid units for B5G/6G," *IEEE Trans. Antennas Propag.*, vol. 71, no. 6, pp. 5457–5462, Jun. 2023.

[2] S. Hong, Y. Kim, and J. Oh, "Automobile laminated glass window embedded transmitarray and ray tracing validation for enhanced 5G connectivity," *IEEE Trans. Antennas Propag.*, vol. 70, no. 8, pp. 6671–6682, Aug. 2022.

[3] Q. Luo, S. Gao, M. Sobhy, and X. Yang, "A hybrid design method for thin-panel transmitarray antennas," *IEEE Trans. Antennas Propag.*, vol. 67, no. 10, pp. 6473–6483, Oct. 2019.

[4] M. Jiang, Z. N. Chen, Y. Zhang, W. Hong, and X. Xuan, "Metamaterial-based thin planar lens antenna for spatial beamforming and multibeam massive MIMO," *IEEE Trans. Antennas Propag.*, vol. 65, no. 2, pp. 464–472, Feb. 2017.

[5] S. L. Liu, X. Q. Lin, Z. Q. Yang, Y. J. Chen, and J. W. Yu, "*W*-band low-profile transmitarray antenna using different types of FSS units," *IEEE Trans. Antennas Propag.*, vol. 66, no. 9, pp. 4613–4619, Sep. 2018.

[6] N. Cho, H. Scott, H. Wang, G. Byun, Y. Park, and I. Park, "Non-uniform metasurface-integrated circularly polarized end-fire dipole array antenna," *J. Electromagn. Eng. Sci.*, vol. 23, no. 2, pp. 29–41, 2023.

[7] J. Oh, "Millimeter-wave thin lens employing mixed-order elliptic filter arrays," *IEEE Trans. Antennas Propag.*, vol. 64, no. 7, pp. 3222–3227, Jul. 2016.

[8] Y. Cao, W. Yang, Q. Xue, and W. Che, "A broadband low-profile transmitarray antenna by using differentially driven transmission polarizer with true-time delay," *IEEE Trans. Antennas Propag.*, vol. 70, no. 2, pp. 1529–1534, Feb. 2022.

[9] Y. Ge, C. Lin, and Y. Liu, "Broadband folded transmitarray antenna based on an ultrathin transmission polarizer," *IEEE Trans. Antennas Propag.*, vol. 66, no. 11, pp. 5974–5981, Nov. 2018.

[10] W. An, S. Xu, F. Yang, and M. Li, "A double-layer transmitarray antenna using Malta crosses with vias," *IEEE Trans. Antennas Propag.*, vol. 64, no. 3, pp. 1120–1125, Mar. 2016.

[11] F. Wu, L. Xiang, J. Wang, K.-M. Luk, and W. Hong, "A hybrid-element approach to design wideband ME-dipole transmitarray with improved aperture efficiency," *IEEE Antennas Wireless Propag. Lett.*, vol. 21, no. 7, pp. 1338–1342, Jul. 2022.

[12] T. Li and Z. N. Chen, "Compact wideband wide-angle polarization-free metasurface lens antenna array for multibeam base stations," *IEEE Trans. Antennas Propag.*, vol. 68, no. 3, pp. 1378–1388, Mar. 2020.

[13] C.-Y. Hsu, L.-T. Hwang, T.-S. Horng, S.-M. Wang, F.-S. Chang, and C. N. Dorny, "Transmitarray design with enhanced aperture efficiency using small frequency selective surface cells and discrete Jones matrix analysis," *IEEE Trans. Antennas Propag.*, vol. 66, no. 8, pp. 3983–3994, Aug. 2018.

[14] C. Xue et al., "An ultrathin, low-profile and high-efficiency metalens antenna based on chain Huygens' metasurface," *IEEE Trans. Antennas Propag.*, vol. 70, no. 12, pp. 11442–11453, Dec. 2022.

[15] A. Clemente, L. Dussopt, R. Sauleau, P. Potier, and P. Pouliguen, "Focal distance reduction of transmit-array antennas using multiple feeds," *IEEE Antennas Wireless Propag. Lett.*, vol. 11, pp. 1311–1314, 2012.

[16] E. G. Plaza et al., "An ultrathin 2-bit near-field transmitarray lens," *IEEE Antennas Wireless Propag. Lett.*, vol. 16, pp. 1784–1787, 2017.

[17] P.-Y. Feng, S.-W. Qu, S. Yang, L. Shen, and J. Zhao, "Ku-band transmitarrays with improved feed mechanism," *IEEE Trans. Antennas Propag.*, vol. 66, no. 6, pp. 2883–2891, Jun. 2018.

[18] P.-Y. Feng, S.-W. Qu, and S. Yang, "Ultrawideband low-profile transmitarray with Vivaldi array feed," *IEEE Trans. Antennas Propag.*, vol. 68, no. 4, pp. 3265–3270, Apr. 2020.

[19] A. Aziz, F. Yang, S. Xu, and M. Li, "A low-profile quad-beam transmitarray," *IEEE Antennas Wireless Propag. Lett.*, vol. 19, no. 8, pp. 1340–1344, Aug. 2020.

[20] A. H. Abdelrahman, P. Nayeri, A. Z. Elsherbeni, and F. Yang, "Single-feed quad-beam transmitarray antenna design," *IEEE Trans. Antennas Propag.*, vol. 64, no. 3, pp. 953–959, Mar. 2016.

[21] S. Li, Z. N. Chen, T. Li, F. H. Lin, and X. Yin, "Characterization of metasurface lens antenna for sub-6 GHz dual-polarization full-dimension massive MIMO and multibeam systems," *IEEE Trans. Antennas Propag.*, vol. 68, no. 3, pp. 1366–1377, Mar. 2020.

[22] Z. Wani, M. P. Abegaonkar, and S. K. Koul, "Thin planar metasurface lens for millimeter-wave MIMO applications," *IEEE Trans. Antennas Propag.*, vol. 70, no. 1, pp. 692–696, Jan. 2022.

[23] G. Li, Y. Ge, and Z. Chen, "A compact multibeam folded transmitarray antenna at Ku-band," *IEEE Antennas Wireless Propag. Lett.*, vol. 20, no. 5, pp. 808–812, May 2021.

[24] F. Zhang, G. Yang, and Y. Jin, "Low-profile circularly polarized transmitarray for wide-angle beam control with a third-order meta-FSS," *IEEE Trans. Antennas Propag.*, vol. 68, no. 5, pp. 3586–3597, May 2020.

[25] P.-Y. Feng, S.-W. Qu, and S. Yang, "Low-profile dipole array fed transmitarray," in *Proc. 10th Global Symp. Millim.-Waves*, pp. 134–136, 2017.

[26] P.-Y. Feng, S.-W. Qu, X.-H. Chen, and S. Yang, "Low-profile high-gain and wide-angle beam scanning phased transmitarray antennas," *IEEE Access*, vol. 8, pp. 34276–34285, 2020.

[27] J. Oh, "Millimeter-wave short-focus thin lens employing disparate filter arrays," *IEEE Antennas Wireless Propag. Lett.*, vol. 15, pp. 1446–1449, 2015.

[28] P.-Y. Feng, S.-W. Qu, and S. Yang, "Octave bandwidth transmitarrays with a flat gain," *IEEE Trans. Antennas Propag.*, vol. 66, no. 10, pp. 5231–5238, Oct. 2018.

[29] R. G. Vaughan, "Polarization diversity in mobile communications," *IEEE Trans. Veh. Technol.*, vol. 39, no. 3, pp. 177–186, Aug. 1990.

[30] B. Lindmark and M. Nilsson, "On the available diversity gain from different dual-polarized antennas," *IEEE J. Sel. Areas Commun.*, vol. 19, no. 2, pp. 287–294, Feb. 2001.

[31] D. A. Cahyasiwi, F. Y. Zulkifli, and E. T. Rahardjo, "Switchable slant polarization filtering antenna using two inverted resonator structures for 5G application," *IEEE Access*, vol. 8, pp. 224033–224043, 2020.

[32] L. Vallozzi, "Patch antenna with slanted ±45° dual polarization and performance comparison with H/V diversity," in *Proc. 10th Eur. Conf. Antennas Propag. (EuCAP)*, Apr. 2016, pp. 1–5.

[33] S. Dey and S. Dey, "Conformal miniaturized angular stable triband frequency selective surface for EMI shielding," *IEEE Trans. Electromagn. Compat.*, vol. 64, no. 4, pp. 1031–1041, Aug. 2022.

[34] G. Venkatesh, M. Thottappan, and S. P. Singh, "Highly angularly stable dual-band stop FSS for blocking satellite downlink frequencies," *IEEE Trans. Electromagn. Compat.*, vol. 64, no. 6, pp. 2055–2059, Dec. 2022.

[35] P. Nayeri, F. Yang, and A. Z. Elsherbeni, *Reflectarray Antennas: Theory, Designs, and Applications*. Wiley, Feb. 2018, p. 432.

[36] C. Yann, R. Loison, R. Gillard, M. Labeyrie, and J.-P. Martinaud, "A new approach combining surrounded-element and compression methods for analyzing reconfigurable reflectarray antennas," *IEEE Trans. Antennas Propag.*, vol. 60, no. 7, pp. 3215–3221, Jul. 2012.

[37] M.-A. Milon, D. Cadoret, R. Gillard, and H. Legay, "Surrounded-element' approach for the simulation of reflectarray radiating cells," *IET Microw., Antennas Propag.*, vol. 1, no. 2, p. 289, 2007.

[38] J. Y. Lau and S. V. Hum, "Analysis and characterization of a multipole reconfigurable transmitarray element," *IEEE Trans. Antennas Propag.*, vol. 59, no. 1, pp. 70–79, Jan. 2011.

[39] M. A. Al-Joumayly and N. Behdad, "Low-profile, highly-selective, dual-band frequency selective surfaces with closely spaced bands of operation," *IEEE Trans. Antennas Propag.*, vol. 58, no. 12, pp. 4042–4050, Dec. 2010.

[40] A. K. Bhattacharyya, *Phased Array Antennas: Floquet Analysis, Synthesis, BFNs, and Active Array Systems*, vol. 179. Hoboken, NJ, USA: Wiley, 2006.

Uichan Park (Graduate Student Member, IEEE) received the B.S. degree in electronic and electrical engineering from Sungkyunkwan University, Suwon, South Korea, in 2020. He is currently pursuing the integrated master's and Ph.D. degrees with the Department of Electrical and Computer Engineering from Seoul National University, Seoul, South Korea.

His current research interests include digital predistortion for RF power amplifiers, RF/mm-wave/microwave integrated circuits, and transmitarray antennas for 5G/6G communication systems.

Jinhyun Kim (Graduate Student Member, IEEE) received the B.S. degree in electrical engineering from Hanyang University, Ansan, Korea, in 2019. He is currently pursuing the Ph.D. degree with Seoul National University, Seoul, South Korea.

His current research interests concern the design of microwave-integrated circuits and reconfigurable intelligence surface systems for 5G/6G communication and brain stimulation.

Taeyeong Yoon (Graduate Student Member, IEEE) received the B.S. degree (summa cum laude) in electronic engineering from Korea Aerospace University, Goyang, South Korea, in 2021, and the M.S. degree from the Department of Electrical and Computer Engineering from Seoul National University, Seoul, South Korea, in 2023, where he is currently pursuing the Ph.D. degree.

His current research interests include suppressing dual-polarized multipath coupling, dual-polarized antennas for sub-6 GHz applications, high-efficiency power amplifiers for millimeter-wave (mm-wave) applications, and RF/mm-wave/microwave integrated circuits.

Haeseung Lee (Member, IEEE) received the B.S. and M.S. degrees in electrical engineering from Yonsei University, Seoul, South Korea, in 2012 and 2014, respectively.

He was with the Agency for Defense Development, Seosan, South Korea, from 2014 to 2017 as an On-Duty Researcher. Since 2018, he has been working at Global Technology Research, Samsung Electronics, Company Ltd., Suwon, South Korea. His research interests include metamaterial/metasurface, antenna design, and RF measurement systems.

Kyungho Yoo (Member, IEEE) received the B.S. degree in electrical and computer engineering from Hanyang University, Seoul, South Korea, in 2002, the M.S. degree in electrical engineering from Seoul National University, Seoul, in 2004, and the Ph.D. degree in electrical engineering from The Pennsylvania State University, University Park, PA, USA, in 2010.

He joined the DMC Research Center, Samsung Electronics, Company Ltd., Suwon, South Korea, in 2010. Since 2015, he has been working at the Global Technology Research, Samsung Electronics. His research interests include the area of 5G array antenna design and modeling and test measurements for wireless communication systems.

Jungsuek Oh (Senior Member, IEEE) received the B.S. and M.S. degrees from Seoul National University, Seoul, South Korea, in 2002 and 2007, respectively, and the Ph.D. degree from the University of Michigan at Ann Arbor, Ann Arbor, MI, USA, in 2012.

From 2007 to 2008, he was with Korea Telecom as a Hardware Research Engineer, working on the development of flexible RF devices. In 2012, he was a Post-Doctoral Research Fellow at the Radiation Laboratory, University of Michigan. From 2013 to 2014, he was a Staff RF Engineer with Samsung Research America, Dallas, TX, USA, working as a project leader for the 5G/millimeter-wave antenna system. From 2015 to 2018, he was a Faculty Member at the Department of Electronic Engineering, Inha University in South Korea, Incheon, South Korea. He is currently an Associate Professor with the School of Electrical and Computer Engineering, Seoul National University. He has published more than 50 technical journal and conference papers. His research interests include mmWave beam focusing/shaping techniques, antenna miniaturization for integrated systems, and radio propagation modeling for indoor scenarios.

Dr. Oh is the recipient of the 2011 Rackham Predoctoral Fellowship Award at the University of Michigan. He has served as a Technical Reviewer for IEEE TRANSACTIONS ON ANTENNAS AND PROPAGATION and IEEE Antenna and Wireless Propagation Letters. He has served as a TPC Member and as a Session Chair for the IEEE AP-S/USNC-URSI and ISAP.